



# Al<sub>8</sub>Mn<sub>5</sub> Particle Settling and Interactions with Oxide Films in Liquid AZ91 Magnesium Alloys

L. PENG<sup>1,5</sup>, G. ZENG,<sup>2</sup> T.C. SU,<sup>1</sup> H. YASUDA,<sup>3</sup> K. NOGITA,<sup>4</sup> and C.M. GOURLAY<sup>1,6</sup>

1.—Department of Materials, Imperial College London, London SW7 2AZ, UK. 2.—School of Materials Science and Engineering, Central South University, Changsha 410083, China. 3.—Department of Materials Science and Engineering, Kyoto University, Kyoto 606-8501, Japan. 4.—School of Mechanical and Mining Engineering, The University of Queensland, Brisbane, QLD 4072, Australia. 5.—e-mail: liuqing.peng15@imperial.ac.uk. 6.—e-mail: c.gourlay@imperial.ac.uk

Al<sub>8</sub>Mn<sub>5</sub> particles form as primary solidification phases in Mg-Al-based alloys and are important for ensuring adequate corrosion resistance. However, excessive Al<sub>8</sub>Mn<sub>5</sub> formation above the  $\alpha$ -Mg liquidus temperature can lead to sludge formation, and the clustering of Al<sub>8</sub>Mn<sub>5</sub> particles on oxide films can generate deleterious casting defects. Here, we use analytical SEM and real-time synchrotron x-ray radiography to study Al<sub>8</sub>Mn<sub>5</sub> particle settling, the formation of a sludge layer, and the mechanism of Al<sub>8</sub>Mn<sub>5</sub> clustering on oxides in AZ91 containing two Fe levels. It is shown that settling Al<sub>8</sub>Mn<sub>5</sub> can become trapped in entrained oxide and that new Al<sub>8</sub>Mn<sub>5</sub> particles also seem to nucleate on oxide films. On cooling, these Al<sub>8</sub>Mn<sub>5</sub> particles continue to grow, creating large Al<sub>8</sub>Mn<sub>5</sub> clusters.

## INTRODUCTION

Automotive magnesium alloys are traditionally Mg-Al-based alloys containing  $\alpha$ -Mg and Mg<sub>17</sub>Al<sub>12</sub> as the major phases.<sup>1</sup> The corrosion performance of these alloys depends to a large degree on the levels of Cu, Ni, Co and Fe,<sup>2–4</sup> which introduce intermetallic compounds that are potent local micro-cathodes in the  $\alpha$ -Mg matrix, and on the level of Mn which combats impurity Fe.<sup>5</sup> To ensure adequate corrosion resistance, the Cu, Ni, and Co content must be kept low, and 0.15–0.3 wt.% Mn is usually added to tie up the impurity Fe in manganese aluminides, which have closer galvanic corrosion potential to  $\alpha$ -Mg than do Fe-rich phases.<sup>6</sup> However, these Mn additions are sufficiently concentrated to cause Al-Mn(-Fe) particles to be stable above the  $\alpha$ -Mg liquidus temperature<sup>7</sup> and, therefore, they need to be considered during melt handling. A further consideration is that liquid Mg-Al alloys are commonly melted, ladled and/or poured in steel containers and, despite the low solubility of Fe in liquid Mg-Al alloys, Fe can be picked up by the melt. For example, in high-pressure die casting, liquid alloy is held for many hours in a steel crucible/pot above the

$\alpha$ -Mg liquidus temperature, and variations in melt temperature during ingot charging and reaction between the steel and liquid alloy create Al-Mn(-Fe) particles that settle to the bottom of the crucible and create die-casting sludge.<sup>8,9</sup> In the direct chill (DC) casting of Mg-Al-based alloys, temperature fluctuations and reaction between the steel launder system and liquid alloy can create Al-Mn(-Fe) particles that can block filters and/or agglomerate into clusters that can become engulfed in the final ingot.<sup>10</sup> While there is a large body of industrial know-how on methods to control Al-Mn(-Fe) particle formation, there is limited scientific understanding on Fe pick-up, and the nucleation, growth and settling of Al-Mn(-Fe) particles, and a deeper understanding is required to minimise the build-up of die-casting sludge and prevent large Al-Mn(-Fe) clusters from entering castings.

Similar to most cast metals, magnesium alloys can contain entrained oxide films,<sup>11,12</sup> although, in the case of Mg alloys, the surface film tends to contain MgF<sub>2</sub> as well as oxides due to the use of fluorine-containing protective cover gases.<sup>13,14</sup> Past work has shown that, in the DC casting of Mg alloy AZ80, entrained oxides are often associated with

clusters of large  $\text{Al}_8\text{Mn}_5$  intermetallic particles.<sup>10</sup> Since oxides and large brittle intermetallics are deleterious to tensile ductility and fatigue life,<sup>10,11,15</sup> it is important to understand how  $\text{Al}_8\text{Mn}_5$  particles cluster around entrained oxides. One aim of this work is to elucidate the IMC clustering mechanism on entrained oxides and provide new insights that could enable the prevention of these defects in DC cast ingots.

To address these questions, first we explore how Fe pick-up from steel crucibles affects Al-Mn(-Fe) phase formation. We then perform in situ x-ray analysis of Al-Mn(-Fe) particle behavior above the  $\alpha$ -Mg liquidus temperature in low-Fe AZ91 and in AZ91 that has picked-up Fe from a mild steel crucible, with a focus on settling, sludge formation, and interactions with entrained oxides.

## METHODS

The starting material for this study was AZ91; its composition given in Table I is also similar to the wrought alloy AZ80. This alloy was studied in two forms: (1) AZ91 cut directly from commercial ingot or remelted in  $\text{Al}_2\text{O}_3$  crucibles and (2) AZ91 that had picked-up Fe by melting in a steel crucible to mimic Fe pick-up in industrial melts. For the Fe pick-up procedure, 2 g of AZ91 was melted and held at 700°C for 4 h in uncoated Fe-0.2C cylindrical crucibles with dimensions of inner diameter of 12 mm and inner height of 18 mm, within sealed quartz tubes backfilled with Ar. A similar procedure involving an  $\text{Al}_2\text{O}_3$  crucible in quartz tubes was used to generate equivalent microstructures without Fe pick-up. The samples were then solidified by placing the 700°C quartz tubes in the vertical cylindrical hole of a steel mold at room temperature. The cooling rate in the range 700–650°C was measured as  $\sim 4$  K/s. The composition of the mild steel crucibles is given in Table I.

The microstructure of Al-Mn(-Fe) IMC particles was examined by analytical scanning electron microscopy (SEM). Cross-sections were prepared by standard metallographic procedures and, immediately after polishing, SEM investigation was performed using a Zeiss Sigma-300. Backscattered electron (BSE) images were taken with an accelerating voltage of 10 kV and a working distance of

10 mm. Electron backscattered diffraction (EBSD) was carried out using 20 kV accelerating voltage and 15 mm working distance, with a 120-mm aperture, the sample tilted at 70°, and a BRUKER e-FlashHR EBSD detector. To reveal the 3-dimensional (3D) morphology of the Al-Mn(-Fe) intermetallics,  $\alpha$ -Mg was selectively dissolved from some samples using a solution of 10% nitric acid in ethanol followed by imaging of the particles in secondary electron mode with an accelerating voltage of 5 kV and a working distance of 5 mm.

For thin-sample x-ray radiography experiments,  $5.8 \times 6.0 \text{ mm} \times 0.16 \text{ mm}$  slices were cut from both the AZ91 ingot and the AZ91 in steel crucibles. Figure 1a shows schematically the resulting thin sample of AZ91 with the Fe-0.2C crucible on two sides. Samples such as Fig. 1a were then placed in the melting/solidification cell in Fig. 1b where 150- $\mu\text{m}$ -thick single crystal MgO sheets were used as confining sheets and as a spacer with a cavity to house the sample and prevent melt reactions with the container. This sandwich was then secured within thicker boron nitride plates and incorporated into a furnace setup on beamline 20XU at the SPring-8 synchrotron. Further details of the beamline, hutch and furnace configuration is given in references.<sup>16–18</sup>

Radiography experiments were performed with a 13-keV x-ray energy. The specimen and cell were heated and melted at a constant rate of 0.5 K/s and subsequently cooled at a constant rate of either 0.083 or 0.5 K/s. During heating and cooling, transmitted x-ray images were recorded at a rate of 2.5 frames per second, with a field of view (FoV) of  $2048 \times 2048$  pixels, corresponding to  $1.0 \text{ mm} \times 1.0 \text{ mm}$ . A flat field correction was applied using dark and flat field images which were recorded separately during the experiments. Image processing and analysis were performed using Matlab and ImageJ. The temperature was calibrated against the melting of eutectic  $\text{Mg}_{17}\text{Al}_{12}$  and the melting of  $\alpha$ -Mg on heating.

## RESULTS AND DISCUSSION

### Primary Al-Mn(-Fe) Particles

Figure 2 shows the typical features of primary Al-Mn(-Fe) intermetallics from the AZ91 melted in

**Table I. Chemical compositions of the materials used**

Alloy	Composition (wt.%)							
	Mg	Al	Zn	Mn	Cu	Si	Ni	Fe
AZ91	Bal.	8.95	0.72	0.19	0.001	0.039	< 0.001	< 0.001
Mild steel crucible		Fe	C	Mn	Si	P	S	
		Bal.	0.2	0.9	0.35	0.05	0.05	

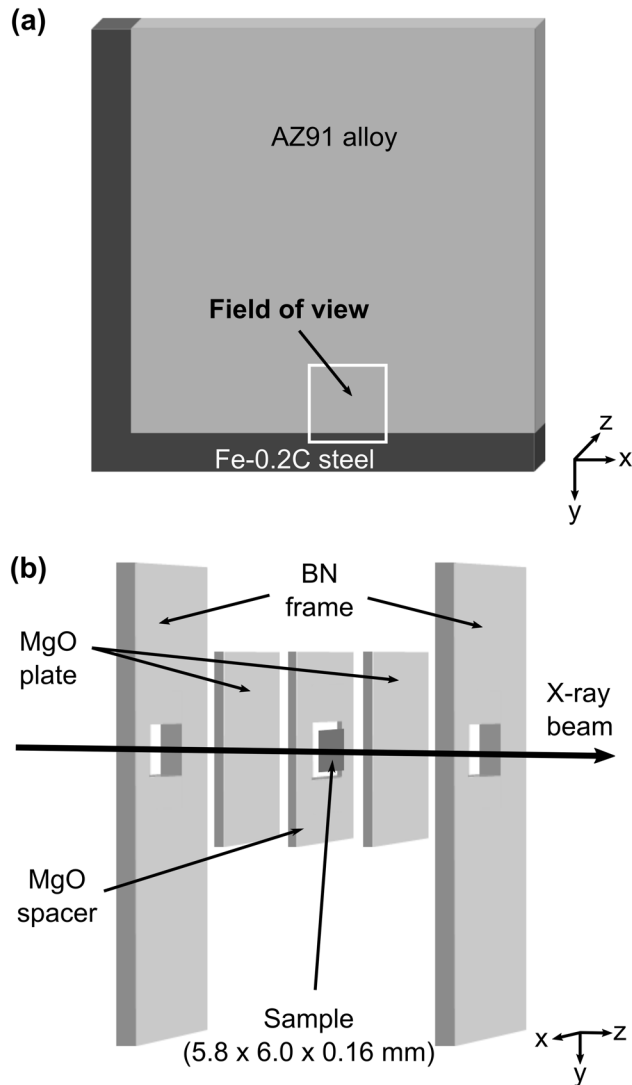


Fig. 1. Experimental set-up for x-ray imaging: (a) polished thin sample and the field of view; (b) geometry of the solidification cell that was incorporated into a furnace on BL20XU at the SPring-8 synchrotron.

Al<sub>2</sub>O<sub>3</sub> and the AZ91 held at 700°C in uncoated Fe-0.2 for 4 h. In both cases, the Al-Mn(-Fe) intermetallics are faceted polyhedral particles. Examining the BSE-SEM images and EBSD phase maps, it can be seen that the particle from AZ91 melted in Al<sub>2</sub>O<sub>3</sub> is single phase Al<sub>8</sub>Mn<sub>5</sub>. In contrast, the particle from AZ91 melted in mild steel is two-phase with a B2-Al(Mn,Fe) core and an Al<sub>8</sub>Mn<sub>5</sub> shell. The structures used for EBSD indexing were from Ref. 19 for Al<sub>8</sub>Mn<sub>5</sub> and the CsCl structure for the B2 phase (e.g., Refs. 20 and 21). These phases can be readily distinguished by EBSD as shown in Ref. 22. For the Fe pick-up sample, EDS point analysis in multiple particles gave compositions of 45Al-34Mn-21Fe ( $\pm 1$  at.%) for B2 and 54Al-40Mn-6Fe ( $\pm 1$  at.%) for Al<sub>8</sub>Mn<sub>5</sub>, showing that the impurity Fe is concentrated in the B2 core phase which is surrounded by a Al<sub>8</sub>(Mn,Fe)<sub>5</sub> shell of lower Fe

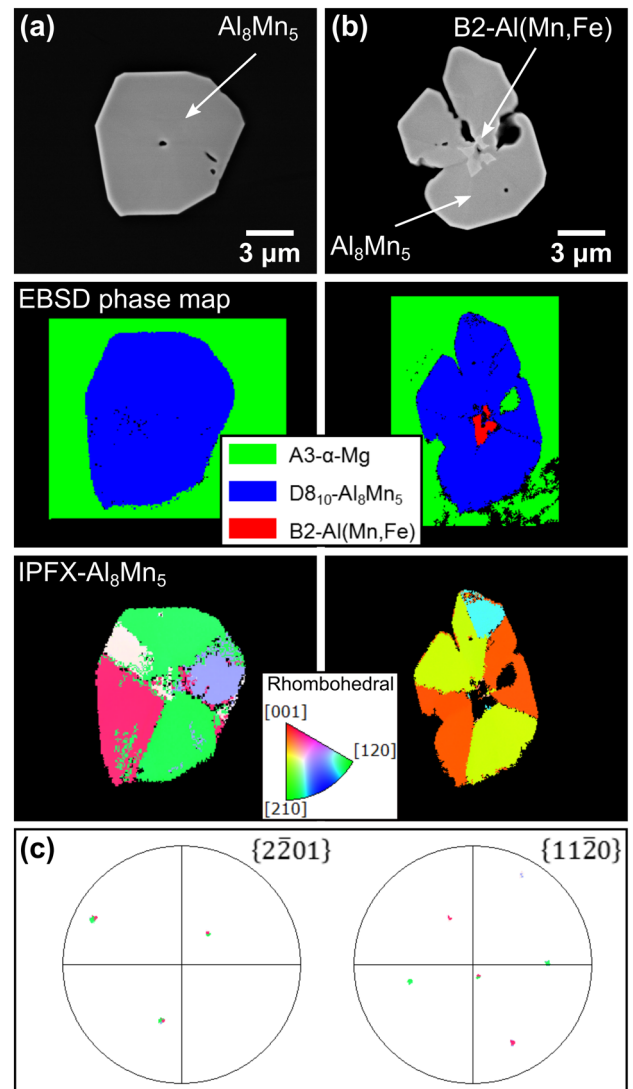


Fig. 2. Typical cross-sections of primary Al-Mn(-Fe) particles in AZ91 after 4 h isothermal holding at 700°C in (a) an Al<sub>2</sub>O<sub>3</sub> crucible and (b) a mild steel crucible. In (a) and (b), the top are BSE-SEM images, the middle are corresponding EBSD phase maps and the bottom are IPF-X maps. (c) Pole figures for two families of planes from the sample in (a) showing cyclic twinning.

content. Previous work by Zeng et al.<sup>22</sup> identified an Fe-containing B2 core phase within primary Al<sub>8</sub>Mn<sub>5</sub> in various batches of AZ91 ingot, but, in that work, the B2 cores were usually small and difficult to find without serial sectioning with a focused ion beam. In the present study, Fe pick-up from the mild steel crucible was sufficient for a clear B2 core to be present in most random cross-sections of primary Al-Mn(-Fe) particles.

Similar to the work of Zeng et al.,<sup>22</sup> it was found here that most primary Al<sub>8</sub>Mn<sub>5</sub> particles were cyclic twinned with up to four orientations in each particle. This can be seen in the EBSD IPF-X maps at the bottom of Fig. 2a and b. Despite some misindexing, the presence of four orientations with linear interfaces between them can be seen clearly in the IPF-X maps. The cyclic twin orientation relationship (OR)

can be identified in the pole figures in Fig. 2c both of which come from the single-phase  $\text{Al}_8\text{Mn}_5$  particle in Fig. 2a; note that all four rhombohedral orientations (colors) overlap at each spot in the  $\{2-201\}$  pole figure giving the impression of only three spots, and each spot in the  $\{11-20\}$  pole figure contains two overlapping orientations (colors). Further information on cyclic twinning in  $\text{Al}_8\text{Mn}_5$  and the OR between the  $\text{Al}_8\text{Mn}_5$  shell and B2 core is given in Ref. 22, where it is shown that  $\{2-201\}$  are the cyclic twin planes and each orientation is  $\sim 90^\circ$  rotated around the three common  $\langle 1-102 \rangle$  axes. The particle in Fig. 2b has the same cyclic twinned structure but only three orientations are present in the cross-section (details not shown here).

Figure 3 shows the typical 3D shapes of primary  $\text{Al}_8\text{Mn}_5$  after  $\alpha$ -Mg was selectively etched away. The particles in Fig. 3a and b are from AZ91 melted in steel and most likely contain a B2-core phase, whereas those in Fig. 3c are from AZ91 melted in  $\text{Al}_2\text{O}_3$ . In both cases, the  $\text{Al}_8\text{Mn}_5$  particles have numerous well-developed facets. Some facets have grooves across them which are likely to be where a twin boundary intersects the surface, based on previous research.<sup>22</sup> For AZ91 melted in  $\text{Al}_2\text{O}_3$ , the primary  $\text{Al}_8\text{Mn}_5$  were all equiaxed polyhedral similar to those in Fig. 3c. In AZ91 melted in steel, there was more variety in the primary  $\text{Al}_8\text{Mn}_5$  morphology, with some  $\text{Al}_8\text{Mn}_5$  having a simple equiaxed polyhedral shape similar to that in Fig. 3b and others having more complex shapes, such as that in Fig. 3a. Occasionally, samples were found to contain entrained oxide and, in these cases, it was common for  $\text{Al}_8\text{Mn}_5$  to be attached to the oxide as shown in Fig. 3c.

The particles in Figs. 2a, b and 3a, b, c span the range of Fe contents that are common in industrial AZ91 and AZ80, from very low ( $< 10$  ppm) Fe in Figs. 2a and 3c to a melt near-saturated in Fe at  $700^\circ\text{C}$  in Figs. 2b and 3a, b. These extremes in Fe content were next used in an x-ray imaging study of the effect of particle size and Fe content on the settling behavior of Al-Mn(-Fe) particles, and the samples containing entrained oxide (e.g., Fig. 3c) were used to study interactions between  $\text{Al}_8\text{Mn}_5$  and oxides.

### $\text{Al}_8\text{Mn}_5$ Particle Settling and Sludge Formation

Figure 4 overviews the x-ray radiography of AZ91 in mild steel during heating at a constant rate of  $0.5$  K/s from fully solid to  $680^\circ\text{C}$ . In Fig. 4a, the sample is fully solid, the  $\alpha$ -Mg dendrites and eutectic  $\text{Mg}_{17}\text{Al}_{12}$  can be observed, and the dark particles distributed in the bulk are mainly  $\text{Al}_8\text{Mn}_5$ . The mild steel appears as the darkest region at the bottom of the FoV due to its lowest transmissivity for x-rays. Note that the volume fraction of Al-Mn(-Fe) particles is much lower than it appears at a first glance because, in radiographic imaging, all the

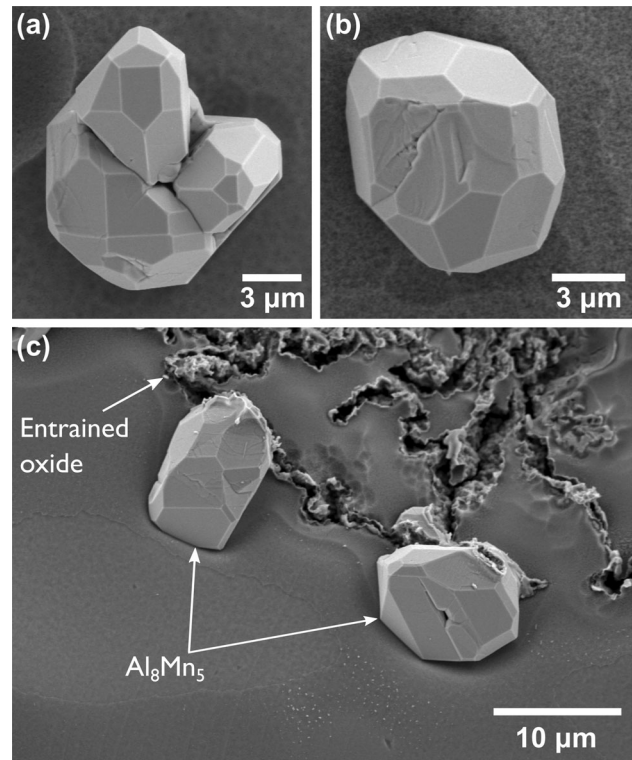
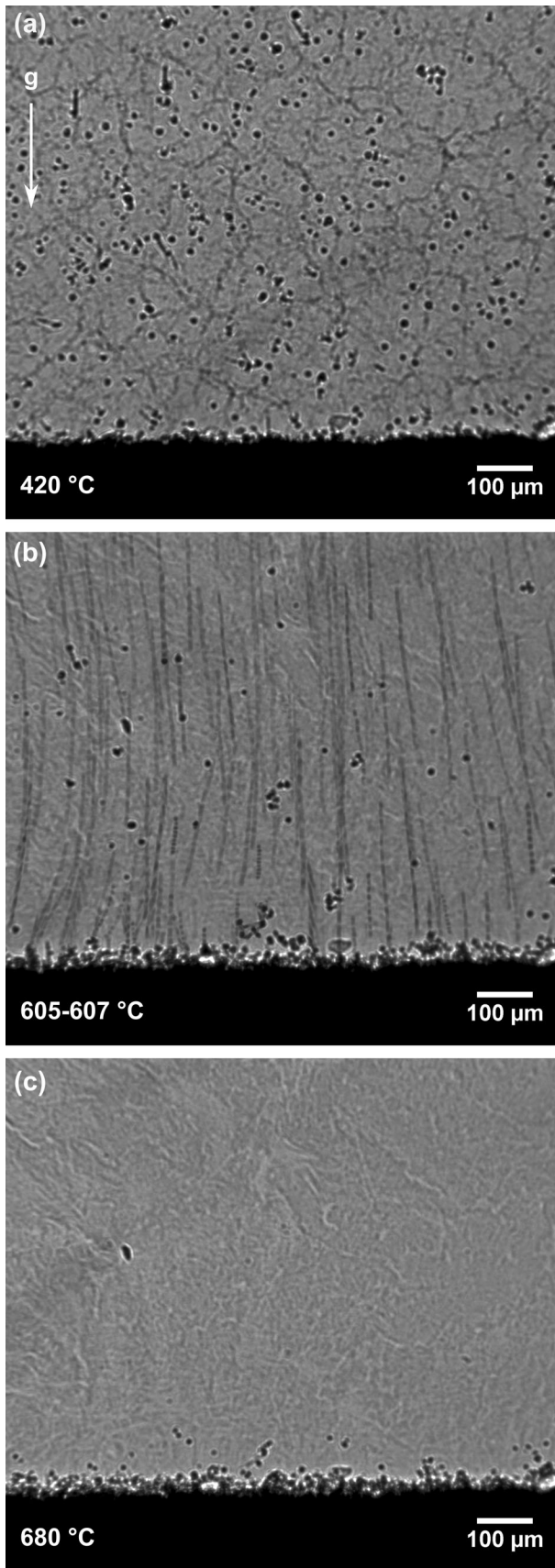


Fig. 3. Typical 3D morphologies of primary  $\text{Al}_8\text{Mn}_5$  particles in AZ91 (a, b) melted in a mild steel crucible at  $700^\circ\text{C}$ , (c) melted in  $\text{Al}_2\text{O}_3$ .

particles in the volume are projected onto the detector to produce a single image. According to thermodynamic calculations in Thermo-Calc TCMG4.0, the volume fraction of Al-Mn(-Fe) particles is less than  $0.25$  vol.% after Scheil solidification. Figure 4b is a 9-frame time-averaged image for the temperature range  $605$ – $607^\circ\text{C}$  during heating in which the  $\alpha$ -Mg is fully melted and  $\text{Al}_8\text{Mn}_5$  particles are freely settling. This time-averaged image shows the trajectory of settling  $\text{Al}_8\text{Mn}_5$  particles in liquid AZ91. Note that the stationary  $\text{Al}_8\text{Mn}_5$  particles are attached to the  $\text{MgO}$  surface. It can be seen from the trajectories in Fig. 4b that there is a zone near the bottom of the crucible where many particles change direction. This indicates that there is significant convection in the liquid here. As the temperature increases to  $680^\circ\text{C}$ , in Fig. 4c, some of the particles have melted but a significant number remain in a settled layer of sludge at the bottom of the crucible and, in contrast, the main body of liquid is almost free of Al-Mn(-Fe) particles. Note that, in this x-ray experiment, the  $\text{Al}_8\text{Mn}_5$  and B2-Al(Mn,Fe) phases cannot be distinguished.

Figure 5 overviews the formation of a sludge layer at the bottom AZ91/mild steel interface during the heating process. The original microstructure of the interfacial layer is given in Fig. 5a where  $\alpha$ -Mg dendrites are partially melted at  $550^\circ\text{C}$  but still prevent the  $\text{Al}_8\text{Mn}_5$  particles from falling. After settling commences, in Fig. 5b, the settled  $\text{Al}_8\text{Mn}_5$  particles pile up at the interface and gradually pack





◀ Fig. 4. X-ray radiography of Al<sub>8</sub>Mn<sub>5</sub> particle behavior during slow heating at 0.5 K s<sup>-1</sup> up to 680°C. (a) Microstructure at 420°C prior to eutectic melting. Al-Mn-based IMCs are dark particles. (b) 9-frame time-averaged image showing Al<sub>8</sub>Mn<sub>5</sub> particle settling at 605–607°C; the stationary particles are Al<sub>8</sub>Mn<sub>5</sub> attached to the MgO surface. (c) Sludge layer of settled Al<sub>8</sub>Mn<sub>5</sub> particles beneath liquid AZ91 at 680°C.

into a sludge layer. As Fig. 5c shows, the sludge layer builds up to a maximum thickness at 638°C. After that, the Al<sub>8</sub>Mn<sub>5</sub> particles and the sludge layer start to shrink due to melting as the temperature continues to increase. Figure 5d shows the microstructure of the sludge layer after 232 s of isothermal holding at 680°C. It can be seen that the thickness and grayscale of the sludge layer noticeably reduces, indicating that the Al-Mn(-Fe) particles partially dissolved into the liquid during isothermal holding at 680°C. The combination of Figs. 4 and 5 show the complex behavior of Al-Mn(-Fe) particles during the melting of ingots and highlights the importance of the heating rate when melting AZ91 ingots. The very slow heating rate of 0.5 K/s used here generates a sludge layer which will reduce the Mn and Fe content of the bulk liquid away from the layer, while a rapid heating rate may be able to prevent significant particle settling during melting. Similar settling and sludge formation would be expected when the temperature drops due to new ingots being charged to a crucible.

Past studies on particle or grain settling in various aspects of solidification processing, including in grain refiner fade<sup>23,24</sup> and gravity macrosegregation,<sup>25,26</sup> have used Stoke's law and its variations to study settling. To obtain a quantitative understanding of Al-Mn(-Fe) settling, 43 particles that settled freely without obvious interaction with neighboring particles were selected for tracking in the radiograph sequences in datasets from AZ91 in mild steel and AZ91 held in MgO. The particle height (vertical position above the bottom boundary) versus time data is plotted for selected particles in Fig. 6a using object tracking in ImageJ. It can be seen that all the particles have a near-constant velocity (slope) when the particles are at positions more than ~ 160 μm from the bottom of the sample. Within 160 μm of the bottom, many Al<sub>8</sub>Mn<sub>5</sub> particles decelerated before reaching the bottom of Fig. 6a, which correlates well with the observed zone near the bottom of the crucible where many particles change direction in the time-averaged image in Fig. 4b, and indicates an upward liquid flow near the bottom driven by particle settling and bottom boundary effects as studied in Ref. 25. Based on this, all particle settling data were taken from the near-constant velocity region more than 160 μm above the bottom of the sample/crucible.

The particle diameter was measured using the transmitted x-ray intensity profile across a particle. It was defined as the width of the valley in which

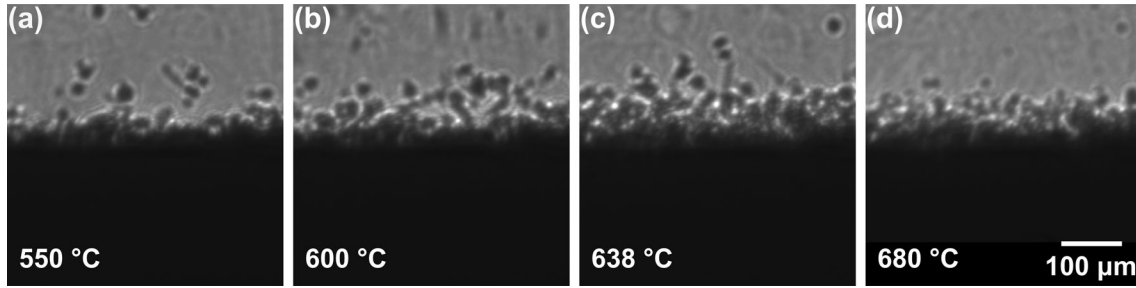


Fig. 5. X-ray radiography of sludge layer formation at the bottom interface during slow heating at  $0.5 \text{ K s}^{-1}$  up to  $680^\circ\text{C}$ : (a) original microstructure of the layer at  $550^\circ\text{C}$  before particle settling; (b) settling of IMC particles at  $600^\circ\text{C}$ ; (c) accumulated particles forming a sludge layer after continued settling at  $638^\circ\text{C}$ ; (d) dissolving of IMC sludge layer as temperature increases to  $680^\circ\text{C}$ .

the intensities are smaller than the intensity of adjacent Mg-rich liquid. The measured  $\text{Al}_8\text{Mn}_5$  particle settling velocity versus diameter data from 43 particles are plotted in Fig. 6b. The settling velocity of  $\text{Al}_8\text{Mn}_5$  particles,  $v_{c,\text{Al}_8\text{Mn}_5}$ , can be compared with the theoretical terminal velocity,  $v_{c,\text{Stokes}}$ , in Eq. 1, which comes from the balance between the frictional force (Stokes' drag) acting on the solid/liquid interface and the weight and buoyancy forces.<sup>27</sup>

$$v_{c,\text{Stokes}} = \frac{(\rho_p - \rho_L)gd_p^2}{18\mu_L} \quad (1)$$

where  $g$  is the gravitational acceleration,  $\rho_p$ ,  $\rho_L$  are the densities of  $\text{Al}_8\text{Mn}_5$  and the Mg-rich liquid,  $d_p$  is the particle diameter, and  $\mu_L$  is the dynamic viscosity of the liquid Mg alloy. The solid line in Fig. 6b is a plot of  $v_{c,\text{Stokes}}$  versus  $d_p$  where JMatPro<sup>®</sup> v.7.0 was used to obtain data for the temperature-dependent dynamic viscosity and density of the liquid in AZ91 at  $607^\circ\text{C}$ , and  $4.43 \text{ g cm}^{-3}$  was used for the density of  $\text{Al}_8\text{Mn}_5$ .<sup>28</sup>

It can be seen in Fig. 6b that Stokes' law overestimates the settling velocity of the  $\text{Al}_8\text{Mn}_5$  particles. It is noted that Eq. 1 is valid for homogeneous (uniform in composition), spherical particles with smooth surfaces under laminar liquid flow relative to the solid, and for particles that do not interact with each other. To consider the settling velocity of non-spherical and not fully-solid particles with wall and inertial effects, the terminal velocity of  $\text{Al}_8\text{Mn}_5$  may be estimated as.<sup>29</sup>

$$v_{c,\text{Al}_8\text{Mn}_5} = v_{c,\text{Stokes}} \frac{g_e \cdot K_\Phi}{K_f} + v_L \quad (2)$$

where  $g_e$  is the volume fraction of solid within the particle envelope.  $K_\Phi$  is the Stokes' shape factor,<sup>30</sup> the settling speed ratio of the particle to the equivalent sphere. This factor represents the effect of the sphericity,  $\Phi$ , of the particle which is defined as the ratio of the surface area of the equivalent sphere to that of the actual particle.<sup>31</sup>  $K_f$  is a correction factor to account for fluid flow effects

from the walls (which are related to the ratio between the particle diameter and sample thickness) and inertial effects (which are related to the particle Reynolds number,  $Re = \rho_L d_p v_{c,\text{Al}_8\text{Mn}_5} / \mu_L$ ).  $v_L$  is the liquid velocity with respect to global coordinates. Equation 2 contains the three main factors causing  $v_{c,\text{Al}_8\text{Mn}_5} < v_{c,\text{Stokes}}$  in Fig. 6b:

1. The correction factor,  $K_f$ , needs to be considered due to the thin-sample geometry used here (Fig. 1a). Here, the ratio between the particle diameter and the sample thickness is generally less than 0.1, and the  $Re \approx 0.01$ . From the polynomial expansion of  $K_f$  given in Ref. 29 and the comparison with dendrite models in Ref. 32,  $1 < K_f < 1.1$  can be estimated.
2. The particles are not spherical, they are polyhedral and sometimes complex (see Figs. 2 and 3). Previous studies<sup>30,33</sup> proposed an empirical relationship,  $K_\Phi \approx \Phi^{0.83}$ , if  $Re < 1$ . Figure 2 shows that each particle has different sphericity,  $\Phi$ . This value may span from  $\sim 0.8$  similar to a cuboid with an aspect ratio near to 1.0<sup>34</sup> to  $\sim 0.9$  similar to a regular dodecahedron.<sup>34</sup> Therefore,  $0.83 < K_\Phi < 0.92$  can be estimated.
3. The  $\text{Al}_8\text{Mn}_5/\text{B2}$  particles are sometimes not fully-solid and can contain some internal liquid channels (see Fig. 2b). Based on measurements of cross-sections such as Fig. 2a and b,  $0.9 < g_e \leq 1.0$  may be expected.

As the  $v_{c,\text{Al}_8\text{Mn}_5}$  data were measured when the particle height was  $> 250 \mu\text{m}$  before the onset of distinctive particle deceleration, the effect of  $v_L$  on the measurement of terminal settling velocities can be neglected. The combined correction factor,  $g_e \cdot K_\Phi / K_f$ , shown in Eq. 2 is expected to be in the range 0.7–0.9 depending on the particle geometry. This evaluated range is in reasonable agreement with the  $0.75 \cdot v_{c,\text{Stokes}}$  line in Fig. 6b (dashed black curve). Equation 2 is also consistent with the significant scatter in the settling data in Fig. 6b: each particle in Figs. 2 and 3 will have its own Stokes' shape factor and volume fraction of solid within its particle envelope.

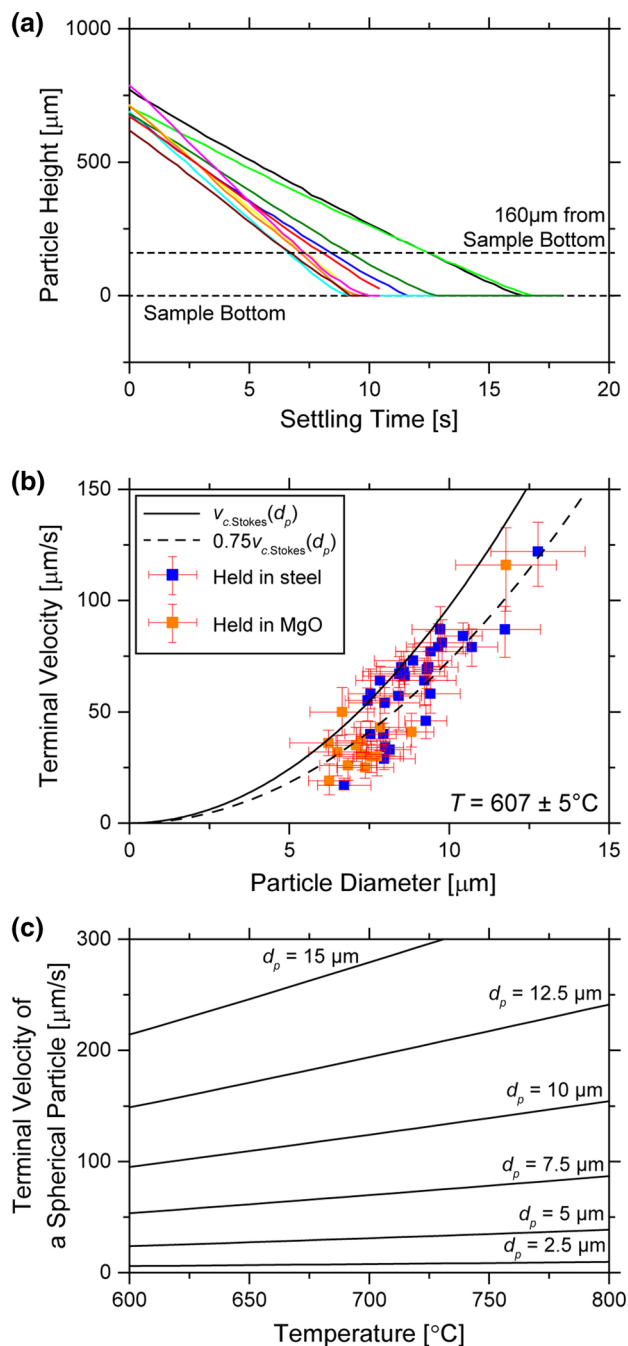


Fig. 6. Analysis of Al-Mn(-Fe) particle settling in liquid AZ91 from x-ray imaging. (a) Tracking of ten Al<sub>8</sub>Mn<sub>5</sub> particles during settling; particle height is the vertical distance between the centroid of the particle and the bottom of the sample. (b) Comparison between theoretical terminal velocity (solid black curve),  $v_{c,Stokes}$ ,  $0.75 \cdot v_{c,Stokes}$  (dashed black curve), and measured terminal velocity,  $v_{c,Al_8Mn_5}$  (orange and blue dots with uncertainty). (c) Theoretical terminal velocity of spheres  $v_{c,Stokes}$  as a function of temperature and the diameter of spherical particles. Note that data in (a) and (b) were measured at  $T = 607^\circ\text{C} \pm 5^\circ\text{C}$ . The temperature-dependent density and viscosity of the liquid in Mg-9Al-0.7Zn-0.15Mn were from JMatPro v.7, and  $\rho_p = \rho_{Al_8Mn_5} = 4.43 \text{ g cm}^{-3}$  was from Ref. 27 (Color figure online).

Figure 6b also shows that there is no significant difference between the settling of Al<sub>8</sub>Mn<sub>5</sub> particles in AZ91 and B2/Al<sub>8</sub>Mn<sub>5</sub> two-phase particles in Fe-

contaminated AZ91. This is likely because the B2 cores are relatively small and the two phases have similar density.

The analysis in Fig. 6a and b is for particles settling at the approximately constant temperature of  $607 \pm 5^\circ\text{C}$ . During heating/cooling, the size of the Al<sub>8</sub>Mn<sub>5</sub> particles changes due to melting/solidification and the Al<sub>8</sub>Mn<sub>5</sub> density, liquid density and liquid viscosity change due to changes in composition and temperature. To capture the combined effects of changing particle size and temperature, the Stokes' terminal velocity for four particle sizes over the relevant temperature range for AZ91 melt handling, 600–800°C, is plotted in Fig. 6c. It can be seen that the Stokes' terminal velocity increases as the temperature increases for a given particle size. This is mostly caused by the reduction of  $\mu_L$  with increasing temperature, since the change in  $\rho_L$  has a relatively small effect (using data from JMatPro® v.7.0) and the role of the change in  $(\rho_p - \rho_L)$  is even smaller since both phases expand on heating. Figure 6c plots the terminal velocity for spheres, and the actual settling velocity of Al<sub>8</sub>Mn<sub>5</sub> particles can be estimated as  $0.75 \cdot v_{c,Stokes}$  based on Fig. 6b.

### Interactions Between Al<sub>8</sub>Mn<sub>5</sub> Particles and Entrained Oxides

AZ91 samples containing entrained oxide such as that in Fig. 3c were used to study Al<sub>8</sub>Mn<sub>5</sub>-oxide interactions. Figure 7 illustrates two interaction behaviors during cooling at 0.5 K/s from 720°C. The oxides appear as bright clusters in x-ray radiography. In Fig. 7a, the AZ91 alloy and Al-Mn(-Fe) particles are both fully melted after isothermal holding at 720°C and the presence of an entrained oxide can be clearly seen. During cooling, Al<sub>8</sub>Mn<sub>5</sub> particles start nucleating in the liquid and begin settling soon after. Figure 7b is a 41-frame time-averaged image showing the trajectory of the falling particles. It can be seen that some particles fall into the entrained oxide and are entrapped by it, while the particles at the side are free falling. Figure 7b is direct evidence that entrained oxides can act as filters, trapping intermetallic particles. Figure 7c and d shows the growth of the trapped Al<sub>8</sub>Mn<sub>5</sub> particles in the oxide during continued cooling (there are also some adjacent particles that nucleated on the sample surface and, therefore, did not settle). From Fig. 7c and d, it can be seen that the Al-Mn(-Fe) particles grow substantially from when they were trapped in the oxide (Fig. 7b and c) to the end of solidification (near Fig. 7d).

Figure 7e, f, g and h shows a different type of interaction between Al<sub>8</sub>Mn<sub>5</sub> and entrained oxide: the apparent nucleation of Al<sub>8</sub>Mn<sub>5</sub> particles on the oxide. In Fig. 7e, the sample is fully melted and the presence of an entrained oxide can be clearly seen. Figure 7f is a 41-frame time-averaged image of the same region, showing the trajectories of settling particles. It can be seen that none of the falling



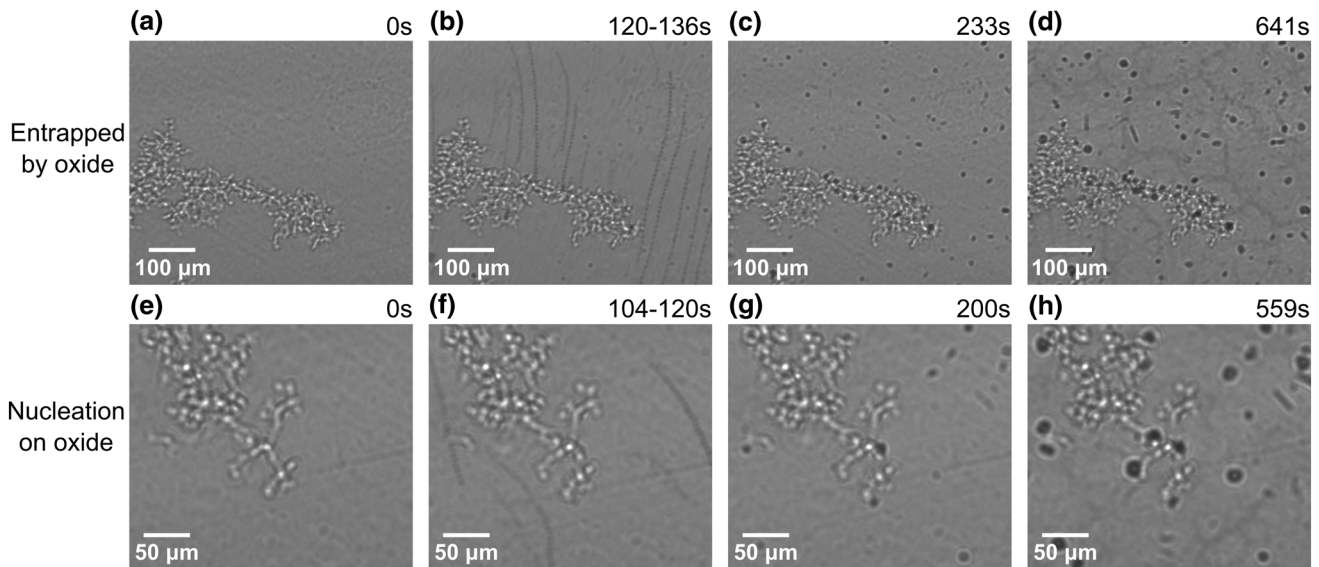


Fig. 7. X-ray radiography of  $\text{Al}_8\text{Mn}_5$  interactions with oxides in liquid AZ91. (a–d) entrapment of  $\text{Al}_8\text{Mn}_5$ : (a) an entrained oxide in liquid AZ91; (b) 41-frame time-averaged image showing settling  $\text{Al}_8\text{Mn}_5$  particles being trapped in the entrained oxide. (c, d) Growth of trapped  $\text{Al}_8\text{Mn}_5$  particles during continued cooling; (c) is above the  $\alpha$ -Mg liquidus temperature, while (d) is close to the nucleation of eutectic  $\text{Mg}_{17}\text{Al}_{12}$ . (e–h) Nucleation of  $\text{Al}_8\text{Mn}_5$  on oxide: (e) an entrained oxide in liquid AZ91; (f) 41-frame time-averaged image showing that this oxide does not trap any settling  $\text{Al}_8\text{Mn}_5$  particles; (g) growth of  $\text{Al}_8\text{Mn}_5$  particles after nucleating on the oxide; (h) further growth of  $\text{Al}_8\text{Mn}_5$  particles during continued cooling. Note that  $\alpha$ -Mg is present in (d) and (h).

$\text{Al}_8\text{Mn}_5$  particles are trapped by this oxide during settling. Shortly afterwards,  $\text{Al}_8\text{Mn}_5$  particles start growing directly on the entrained oxide, as can be seen by comparing Fig. 7f and g and noting the shared interface between various  $\text{Al}_8\text{Mn}_5$  and the oxide. It is likely that these  $\text{Al}_8\text{Mn}_5$  particles nucleated on the oxide, although this cannot be fully confirmed as the imaging only captures  $\sim 0.5 \mu\text{m}$  per pixel. On further cooling, the particles undergo further growth as shown in Fig. 7h.

Figure 8 is a plot of growth measurements of five entrapped  $\text{Al}_8\text{Mn}_5$  particles and six  $\text{Al}_8\text{Mn}_5$  particles that nucleated on the entrained oxide in Fig. 7, where the size of the particles is defined as the equivalent circle diameter. The particle growth behavior is similar irrespective of whether they fell into the oxide or nucleated on it. It can be seen that  $\text{Al}_8\text{Mn}_5$  nucleation on the oxide occurred continuously over a significant period of  $\sim 100$  s, corresponding to  $\sim 50$  K in a near-uniform thermal field. All the particles grew fastest in the early stages and then decelerated until they reached a near-constant size, and the  $\text{Al}_8\text{Mn}_5$  grew mostly before the nucleation of  $\alpha$ -Mg. Note that the growth behavior in Fig. 8 is specific to  $\text{Al}_8\text{Mn}_5$  growth on the entrained oxide and is somewhat different to the free growth of  $\text{Al}_8\text{Mn}_5$  particles in the liquid (not shown here), perhaps because the number density of particles is higher on the entrained oxide and because a large oxide film interferes with the developing solute field around growing  $\text{Al}_8\text{Mn}_5$  particles.

Notice that the final size of  $\text{Al}_8\text{Mn}_5$  particles in Fig. 8 is up to  $30 \mu\text{m}$ , which is much larger than

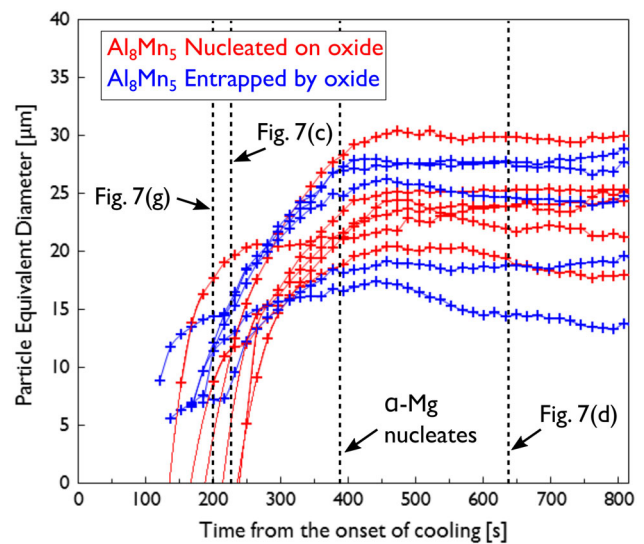


Fig. 8. Quantification of  $\text{Al}_8\text{Mn}_5$  particle growth during cooling from  $720^\circ\text{C}$  at  $0.5$  K/s from the dataset in Fig. 7. Five entrapped  $\text{Al}_8\text{Mn}_5$  particles and six  $\text{Al}_8\text{Mn}_5$  particles that nucleated on the entrained oxide are shown.

those in Figs. 2, 3 and 6. This is because the data in Figs. 7 and 8 are from a sample cooled at  $0.5$  K/s on the synchrotron whereas the cooling rate was  $\sim 4$  K/s when the samples were cast in the laboratory. The data in Fig. 6 are from the first heating of laboratory-cast samples in which  $\text{Al}_8\text{Mn}_5$  particles fall freely when the  $\alpha$ -Mg melts, since they are not attached to the sample surface. When samples were solidified in the thin-sample synchrotron cell, most  $\text{Al}_8\text{Mn}_5$  particles nucleated and remained on the sample surface (or entrained oxide when present)



and could not be used for the settling study at  $607 \pm 5^\circ\text{C}$  in Fig. 6. For example, for the dataset in Figs. 7 and 8, after an initial large number of falling particles near the start of cooling in Fig. 7b and f, most new Al<sub>8</sub>Mn<sub>5</sub> particles nucleated and remained on the sample surface where they grew to a large size.

From Figs. 7 and 8, it is likely that the large clusters of Al<sub>8</sub>Mn<sub>5</sub> particles around the entrained oxides sometimes found in DC casting are a consequence of the entrained oxide acting as a filter, capturing falling (or flowing) Al<sub>8</sub>Mn<sub>5</sub> particles followed by further nucleation on the oxide, and the substantial growth of those particles during slow cooling.

### CONCLUSION

The behavior of Al-Mn(-Fe) particles in the melt above the  $\alpha$ -Mg liquidus temperature has been studied by combining analytical SEM with in situ x-ray radiography. The following conclusions can be drawn:

- Fe pick-up from mild steel crucibles held at  $700^\circ\text{C}$  caused the formation of a B2-Al(Mn,Fe) compound, resulting in two-phase Mn-bearing intermetallic particles consisting of a B2 core and a D8<sub>10</sub>-Al<sub>8</sub>Mn<sub>5</sub> shell. At low Fe content (< 10 ppm), the particles were mostly D8<sub>10</sub>-Al<sub>8</sub>Mn<sub>5</sub>.
- For both low-Fe and high-Fe AZ91, primary Al<sub>8</sub>Mn<sub>5</sub> particles were cyclic twinned and contained up to four Al<sub>8</sub>Mn<sub>5</sub> orientations similar to Ref. 22. The particles had equiaxed polyhedral morphology with multiple facets and often contained internal liquid channels.
- In samples containing entrained oxide, it was common for Al<sub>8</sub>Mn<sub>5</sub> particles to be attached to the oxide.
- Al<sub>8</sub>Mn<sub>5</sub> particle settling and sludge formation has been observed directly. The settling data are in reasonable agreement with Stokes' law once correction factors for the thin sample geometry, the non-spherical particles, and the internal liquid channels are accounted for.
- Direct observation has confirmed that entrained oxides can act as filters to Al<sub>8</sub>Mn<sub>5</sub> particles, trapping them as they settle. Separately, Al<sub>8</sub>Mn<sub>5</sub> particles appear to nucleate on entrained oxides. After numerous Al<sub>8</sub>Mn<sub>5</sub> particles have become trapped and/or nucleated on entrained oxides, they continue to grow on cooling, leading to a large cluster of intermetallics.

### ACKNOWLEDGEMENTS

The authors gratefully acknowledge funding from the UK EPSRC Future LiME Hub (EP/N007638/1), a President's scholarship from Imperial College London, and a Grant-in-Aid for Scientific Research (S) (24226018) from JSPS, Japan. Synchrotron

experiments were conducted during SPring-8 beamtime 2017B-1478. We acknowledge the valuable input of Mark Turski and Tim Wilks from Magnesium Elektron early in this project.

### OPEN ACCESS

This article is distributed under the terms of the Creative Commons Attribution 4.0 International License (<http://creativecommons.org/licenses/by/4.0/>), which permits unrestricted use, distribution, and reproduction in any medium, provided you give appropriate credit to the original author(s) and the source, provide a link to the Creative Commons license, and indicate if changes were made.

### REFERENCES

1. A.A. Luo, *J. Magnes. Alloy* 1, 2 (2013).
2. J.P. Hanawalt, C.E. Nelson, and J.A. Peloubet, *Trans. AIME* 147, 273 (1942).
3. C. Blawert, E. Morales, W. Dietzel, and K.U. Kainer, SAE Technical Paper, no. 2006-1-254 (2006).
4. M. Liu, P.J. Uggowitzer, A.V. Nagasekhar, P. Schmutz, M. Easton, G.L. Song, and A. Atrens, *Corros. Sci.* 51, 602 (2009).
5. J.D. Hanawalt and C.E. Nelson, Magnesium base alloy, US patent 2264309A (1941).
6. O. Lunder, K. Nişancıoğlu, and R.S. Hansen, SAE Technical Paper, no. 930755, 117 (1993).
7. Y. Du, J. Wang, J. Zhao, J.C. Schuster, F. Weitzer, R. Schmid-Fetzer, M. Ohno, H. Xu, Z.K. Liu, S. Shang, and W. Zhang, *Int. J. Mater. Res.* 98, 855 (2007).
8. A. Thorvaldsen and D.L. Albright, in *17th International Die Casting Congress and Exposition*, 337 (1993).
9. C.P. Corby, N.J. Ricketts, M. Qian, and R.D. Bailey, *Magnes. Technol.* 2004, 209 (2004).
10. D. Mackie, J.D. Robson, P.J. Withers, and M. Turski, *Mater. Charact.* 104, 116 (2015).
11. W.D. Griffiths and N.W. Lai, *Metall. Mater. Trans. A* 38, 190 (2007).
12. A.R. Mirak, M. Divandari, S.M.A. Boutorabi, and J. Campbell, *Int. J. Cast Met. Res.* 20, 215 (2007).
13. S. Cashion, N. Ricketts, and P. Hayes, *J. Light Met.* 2, 43 (2002).
14. S. Lun Sin, A. Elsayed, and C. Ravindran, *Int. Mater. Rev.* 58, 419 (2013).
15. Y. Xue, M.F. Horstemeyer, D.L. McDowell, H. El Kadiri, and J. Fan, *Int. J. Fatigue* 29, 666 (2007).
16. H. Yasuda, T. Nagira, M. Yoshiya, N. Nakatsuka, A. Sugiyama, K. Uesugi, and K. Umetani, *ISIJ Int.* 51, 402 (2011).
17. T. Nagira, H. Yokota, S. Morita, H. Yasuda, M. Yoshiya, C.M. Gourlay, A. Sugiyama, K. Uesugi, and K. Umetani, *ISIJ Int.* 53, 1195 (2013).
18. G. Zeng, K. Nogita, S. Belyakov, J.W. Xian, S.D. McDonald, K.V. Yang, H. Yasuda, and C.M. Gourlay, *Magnes. Technol.* 2017, 597 (2017).
19. S. Thimmaiah, Z. Tener, T.N. Lamichhane, P.C. Canfield, and G.J. Miller, *Zeitschrift für Krist. Cryst. Mater.* 232, 601 (2017).
20. A.M. Van der Kraan and K.H.J. Buschow, *Physica B+ C* 138, 55 (1986).
21. B. Grushko and G.R. Stafford, *Scr. Metall. Mater.* 31, 1711 (1994).
22. G. Zeng, J.W. Xian, and C.M. Gourlay, *Acta Mater.* 153, 364 (2018).
23. M. Qian, L. Zheng, D. Graham, M.T. Frost, and D.H. StJohn, *J. Light Met.* 1, 157 (2001).
24. P.L. Schaffer and A.K. Dahle, *Mater. Sci. Eng. A* 413-414, 373 (2005).
25. C. Beckermann and C.Y. Wang, *Metall. Mater. Trans. A* 27, 2784 (1996).
26. G. Lesault, *Mater. Sci. Eng. A* 413-414, 19 (2005).

27. H.H. Lamb, *Hydrodynamics*, 6th ed. (Cambridge: Cambridge University Press, 1932), p. 599.
28. M. Ellner, *Metall. Trans. A* 21, 1669 (1990).
29. H.C. De Groh, P.D. Weidman, R. Zakhem, S. Ahuja, and C. Beckermann, *Metall. Trans. B* 24, 749 (1993).
30. H.Y. Xie and D.W. Zhang, *Powder Technol.* 114, 102 (2001).
31. F. Dioguardi and D. Mele, *Powder Technol.* 277, 222 (2015).
32. R. Zakhem, P.D. Weidman, and H.C. De Groh, *Metall. Trans. A* 23, 2169 (1992).
33. E. Pettyjohn and E.B. Christiansen, *Chem. Eng. Prog.* 44, 157 (1948).
34. T. Li, S. Li, J. Zhao, P. Lu, and L. Meng, *Particuology* 10, 97 (2012).

**Publisher's Note** Springer Nature remains neutral with regard to jurisdictional claims in published maps and institutional affiliations.